Journal of the Mechanics and Physics of Solids 124 (2019) 1–9

Contents lists available at ScienceDirect

Journal of the Mechanics and Physics of Solids

journal homepage: www.elsevier.com/locate/jmps

Extreme pseudomagnetic fields in carbon nanocones by simple loads

Zhili Hu, Zhuhua Zhang*, Liren Liu, Wanlin Guo*

State Key Laboratory of Mechanics and Control of Mechanical Structures and Institute of Nanoscience, Nanjing University of Aeronautics and Astronautics, Nanjing 210016, China

ARTICLE INFO

Article history:
Received 22 June 2018
Revised 17 September 2018
Accepted 28 September 2018
Available online 5 October 2018

Keywords:
Graphene
Carbon nanocone
Pseudomagnetic field
Continuum theory
Atomistic simulation

ABSTRACT

Controllable creation of strain pattern in graphene's lattice is ideal for achieving intriguing pseudomagnetic field but remains challenging due to high in-plane stiffness of graphene. Using continuum theory and atomistic simulations, we show that carbon nanocones exhibit a peculiar electromechanical coupling that yields extreme pseudomagnetic fields by simple loads. Vertically pressing the nanocone by ~2% creates well-defined strain pattern that leads electrons to behave as if under the influence of magnetic fields up to 600 Telsa. Moreover, the strain gradient can be tailored by varying the cone's geometry to achieve controlled distribution of pseudomagnetic fields over a large area. Since synthesis of nanocones of various materials has been mature, the proposed approach is further extendable to other two-dimensional materials towards their electronic modulation by inhomogeneous strain.

1. Introduction

Strain engineering has been important in current semiconductor industry for achieving improved device performance and enriched functionality. As a candidate for fabricating next-generation electronic devices, graphene exhibits unusual capability of controlling its electronic structures by mechanical strain (Liu et al., 2004). The electromechanical coupling in graphene is unique because of its massless Dirac-like electronic states that give rise to novel physics via an interplay with strain, and is realistic since it can resist a tensile strain up to 25% before structural breaking (Kim et al., 2009; Liu et al., 2007). One prominent example is that a strain pattern in a graphene lattice can induce a gauge field, which leads charge carriers in graphene to behave as if under the influence of an external magnetic field (Guinea et al., 2010a, 2010b; Kim et al., 2011; Levy et al., 2010; Liu et al., 2007; Low and Guinea, 2010; Yeh et al., 2011; Zhang et al., 2014a; Zhu et al., 2015). The strain-induced pseudo-magnetic (p-mag) field allows not only for novel manipulation of graphene electronics but also for the exploration of carrier dynamics in extreme magnetic fields unattainable in normal laboratories (Levy et al., 2010). To this end, the key point is to hold a definable strain gradient in stiff graphene lattice. Previous approaches include bubbling graphene (Levy et al., 2010), bending (Guinea et al., 2010a; Low and Guinea, 2010) or twisting (Zhang et al., 2014a) sub-micrometer graphene ribbons, shearing circular graphene rings (Abedpour et al., 2011) and stretching trapezoid-like graphene nanoribbons (Zhu et al., 2015). While these approaches can generate extreme p-mag fields, they all need sophisticated techniques for sustaining the strain pattern in graphene and concurrently incur large local strains up to 15% (Zhang et al., 2014a; Zhu et al., 2015). The over-stretched graphene lattice may suffer from plastic deformation in graphene (Yakobson, 1998) and even

* Corresponding authors.
E-mail addresses: chuwazhang@nuaa.edu.cn (Z. Zhang), wlguo@nuaa.edu.cn (W. Guo).

https://doi.org/10.1016/j.jmps.2018.09.037
0022-5096/

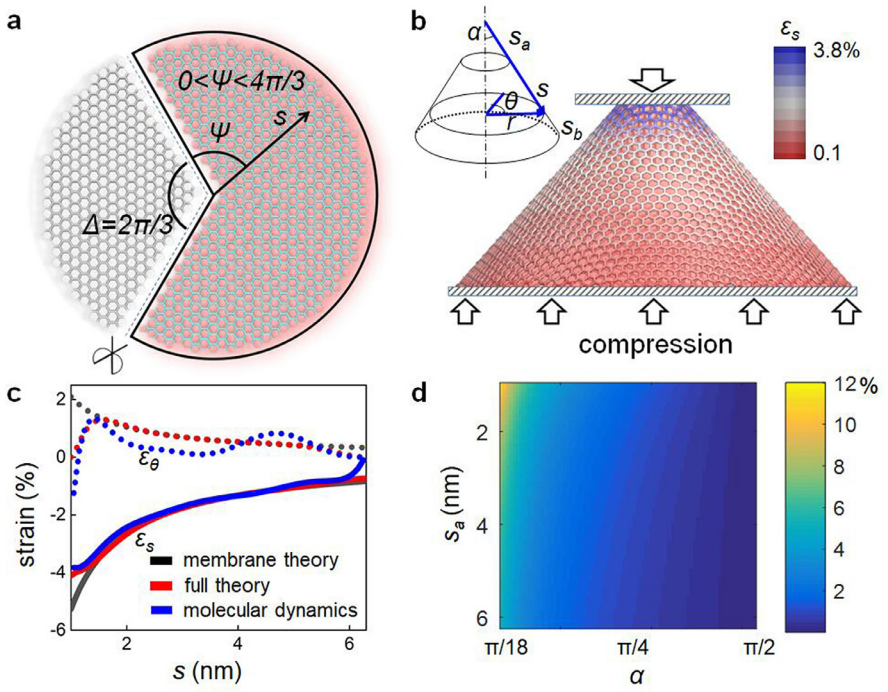

Fig. 1. Geometry and strain pattern of a vertically compressed CNC. (a) A CNC is formed by removing a "wedge" in a circular graphene flake and then stitching two newly created edges. (b) Strain map of a CNC under a 1.8% vertical compression. Top inset illustrates basic geometric parameters, including tapering angle α, meridional coordinate s, and radius of the corresponding cross-section r. (c) Strains ε_s and ε_θ versus s, obtained by different methods. (d) Map of critical ε_{tot} for buckling versus s_a and α, determined by the classical shell theory.

structural breaking (Dumitrica et al., 2006) at raised temperatures during applications. This issue, therefore, underscores the importance of finding a more user-friendly way to realize *p*-mag fields in graphene.

Compared to the planar graphene nanostructures, carbon nanocones (CNCs) (Cano-Marquez et al., 2015; Ghosh et al., 2010; Jaszczak et al., 2003; Kim et al., 2003; Lavin et al., 2002; Lu et al., 2006; Merkulov et al., 2001; Naess et al., 2009; Yang et al., 2005; Yudasaka et al., 2008; Zhang et al., 2003) have a three-dimensional feature that facilitates the exertion of various strains. The CNCs have been actively studied for applications in, for example, electron field emitters (Ghosh et al., 2010) and probes for scanning tunneling microscopy (Cano-Marquez et al., 2015). A number of experiments (Lu et al., 2006; Merkulov et al., 2001; Yang et al., 2005; Zhang et al., 2003) based on chemical vapor deposition methods have synthesized CNCs, whose geometries can be customized using conic catalytic substrates with controlled shape. Here, we employ the CNCs to realize extreme *p*-mag fields in graphene over a large area. A CNC is superior to other nanostructures since it can hold a well-defined strain gradient via the simplest loads: a vertical compression or stretch. Such strain gradient results in *p*-mag fields up to 600 Tesla under a vertical strain of merely 2%. Moreover, hydrostatically inflated CNCs host *p*-mag fields with a uniform distribution along their meridian. These results are likely to inform ongoing effort on the design of nanodevices based on mechanical control over massless Dirac-like electronic structures.

2. Analytical results

2.1. Geometry and general theory

A CNC can be formed by cutting out a "wedge" in a graphene disk and then stitching two open edges (Fig. 1a and b). The tapering angle of the cone can be expressed as $\alpha = \sin^{-1}(1 - \Delta/2\pi)$, where Δ is the disclination angle due to the removed "wedge". The cone's surface is comprised of honeycomb lattice to preserve the Dirac-like electronic character when $\Delta = n\pi/6$ ($n = 1$–5); otherwise, it has a grain boundary along the stitched line. Grain boundaries alter the structure's topology and mechanical behaviors (Wu and Wei, 2013; Zhang et al., 2014b), which will complicate the analysis. We thus focus on these defect-free cones in the following.

For ease of describing the strain field in the CNC, we define a Cartesian coordinate, x axis along the armchair direction of graphene and y along the zigzag direction, see Fig. S1 in the Supporting Information (SI). The strain tensor has three components: ε_x, ε_y and ε_{xy}. The relation between the strain and *p*-mag field can be expressed as (Zhang et al., 2014a; Zhu

et al., 2015),

$$B = \frac{t\beta}{eV_F}\left(\frac{\partial \varepsilon_{yy}}{\partial x} - \frac{\partial \varepsilon_{xx}}{\partial x} - 2\frac{\partial \varepsilon_{xy}}{\partial y}\right), \tag{1}$$

where $\beta = 2.5$ is a dimensionless constant, $t = 2.8$ eV is the hopping energy, and $v_F = 1 \times 10^6$ m/s is the Fermi velocity. We also checked the curvature effect (Fig. S17) (Castro-Villarreal and Ruiz-Sánchez, 2017; Liu, 2018) as well as finite strain effect (Fig. S18) (Ramezani Masir et al., 2013) on the *p*-mag fields, both of which prove to be negligible, as detailed in the section V of the supporting information (SI).

Since Eq. (1) is not straightforward to evaluate *p*-mag fields in a CNC, we set a curvilinear coordinate system (s, θ) for the cone's surface, where s defines the position of a circular cross-section and θ is the angle defining the point position on the circle of the cross-section, as shown in Fig. 1b. The meridian $\theta = 0$ corresponds to the armchair direction. A point (x, y) in the x–y coordinate is translated to ($s = \sqrt{x^2 + y^2}$, $\theta = \psi / \sin\alpha$), where $\psi = \tan^{-1}(y/x)$. Then, the translation between the strain field $\tilde{\varepsilon} = \begin{bmatrix} \varepsilon_s & 0 \\ 0 & \varepsilon_\theta \end{bmatrix}$ in the curvilinear coordinate and ε in the x–y coordinate can be expressed as

$$\varepsilon = A^T \tilde{\varepsilon} A, \tag{2}$$

where the translation matrix is

$$A = \begin{bmatrix} \cos\psi & \sin\psi \\ -\sin\psi & \cos\psi \end{bmatrix}$$

So all strain components in the x–y coordinate can be converted by Eq. (2) to a function of ε_s and ε_θ. Taking these strain components into Eq. (1) results in the *p*-mag field as,

$$B = C\left(\frac{2}{s}\varepsilon_s - \frac{2}{s}\varepsilon_\theta - \varepsilon_s{}' + \varepsilon_\theta{}'\right)\cos 3\psi, \tag{3}$$

where $C = t\beta/ev_F$ is a constant and ψ is the angle between the current and referenced meridians (i.e. $\theta = 0$) after the cone is unfolded to a planar graphene sector (Fig. 1a). Then the next task for calculating B is to solve ε_s and ε_θ under specific loads.

In what follows, we use three levels of methods (Brenner et al., 2002; Cui et al., 2001; Liew et al., 2007; Spagnoli, 2003; Wei and Srivastava, 2004; Xu and Zheng, 2018) to evaluate ε_s and ε_θ in a strained CNC. First, we employ the membrane theory that could result in a simple analytic solution for the *p*-mag field, which is inaccessible using other models. The analytic solution, albeit being inaccurate in describing the fields near the cone's edge, is important to guide the design of field distribution. Thus, the membrane theory serves as a tool of preliminarily evaluating the *p*-mag fields. Full shell theory is then adopted to provide more complicated yet satisfactory evaluation of strain over the whole structure. The results are finally validated by molecular dynamics (MD) simulations. Since the full shell theory compromises the accuracy with reasonable computational cost, the corresponding results will be our focus unless specially noted.

2.2. Membrane theory

First, we study vertically deformed cones. The membrane theory makes the solution simple by ignoring twisting and bending moments in the shell. As such, the non-zero component of in-plane stress is $\sigma_s = \sigma_0/s$ (σ_0 is a constant and $\sigma_0 > 0$ relates to compression) in the s direction as long as the cone is not buckled. Then, ε_s and ε_θ are expressed as

$$\varepsilon_s = \frac{\sigma_s}{E} = \frac{\sigma_0}{Es}, \text{ and } \varepsilon_\theta = -\frac{\nu\sigma_0}{Es}, \tag{4}$$

where E and ν the elastic modulus and Poisson's ratio of graphene, respectively. Eq. (4) dictates that if being compressed, the cone is slightly stretched along the tangent direction while being compressed along the meridian. Moreover, both ε_s and ε_θ decay by s^{-1} (Fig. 1c), indicating that the strains diverge at the cone apex. To avoid this issue, the cone is trimmed at the top in our discussions, like the samples realized in experiments (Hashimoto et al., 2004; Yudasaka et al., 2008). Thus, s is in the $s_a \le s \le s_b$ range, with s_a being the length of the trimmed part and s_b the total length of the cone along the meridian. Therefore, the total strain along s direction can be calculated as,

$$\varepsilon_{tot} = (\sigma_0 ln s_b/s_a)/E. \tag{5}$$

Substituting Eq. (4) into Eq. (3) leads to a concise expression of B as,

$$B = \frac{3C(1+\nu)\sigma_0 \cos 3\psi}{Es^2}, \tag{6}$$

where $\psi = \theta \sin\alpha$. Eq. (6) qualitatively reflects the dependence of B on the cone's geometry.

Second, when the cone is under a hydrostatic pressure, the in-plane stress components can be expressed as

$$N_s = \sigma_s h = sP\tan\alpha/2, \text{ and } N_\theta = \sigma_\theta h = sP\tan\alpha, \tag{7}$$

where P is the outward pressure acting along the normal of cone's surface. By combining Hook's law and Eq. (7), the strain components can be expressed as

$$\varepsilon_s = \frac{sP}{Eh}\left(\frac{1}{2}-\nu\right)\tan\alpha\,,\ \text{and}\ \varepsilon_\theta = \frac{sP}{Eh}\left(1-\frac{\nu}{2}\right)\tan\alpha \tag{8}$$

and

$$\varepsilon_{\text{tot}} = \frac{s_a+s_b}{2}\frac{P}{Eh}\left(\frac{1}{2}-\nu\right)\tan\alpha. \tag{9}$$

By substituting Eq. (8) into Eq. (3), we finally obtain

$$B = \frac{CT(1+\nu)\tan\alpha}{2Eh}\cos 3\psi. \tag{10}$$

2.3. Full theory

The full shell theory is further employed to consider the effect of bending. The full shell theory solution has been detailed in the literature (Liu et al., 1987) and we directly use key results thereof here. Its solution of in-plane stress N is the membrane theory solution plus a correction around the edge,

$$N_{(\bullet)} = N^0_{(\bullet)} + N^c_{(\bullet)}, \tag{11}$$

where $N^0_{(\bullet)}$ is the membrane theory solution, $N^c_{(\bullet)}$ is the correction, and the subscript $(\bullet)$ can be either θ or s. To obtain the correction, the internal force resultants are expressed as a liner combination of Kelvin functions with undetermined coefficients (Liu et al., 1987), as detailed in Eq. (S1) of SI.

For a vertically compressed cone whose top and bottom are fixed, the boundary conditions (BC) are,

$$(\varepsilon^b_\theta+\varepsilon^c_\theta)\,s\sin\alpha = 0|_{s=s_a,s=s_b}\ \text{and}\ V - w^{b'} = 0\Big|_{s=a,s=b}, \tag{13}$$

where $w = \varepsilon_\theta s\tan\alpha - u\tan\alpha$ is the deflection.

For a hydrostatically inflated cone, only the cone's bottom is fixed and the BCs become,

$$(\varepsilon^b_\theta+\varepsilon^c_\theta)\,s\sin\alpha = 0|_{s=b}\ \text{and}\ V - w^{c'} = 0\Big|_{s=b}. \tag{14}$$

Solving Eq. (13) or (14) together with Eq. (S1) obtains coefficients associated with the correction terms N^c_θ and N^c_s. Then, the in-plane stress components N_θ and N_s can be obtained by taking these correction terms into Eq. (11). Dividing N_θ and N_s by h results in σ_θ and σ_s, respectively, and ε_θ and ε_s further by Hook's law. Eventually, the p-mag field B can be calculated by combining the in-plane strains with Eq. (3). Since B is too complicated to be expressed here, we will present its numerical results only.

2.4. Critical loads

The above deductions are valid only for unbuckled cones. While the cone under vertical stretch or hydrostatic inflation does not suffer from buckling issue, possible buckling under vertical compression or hydrostatic compression needs to be carefully examined. In the case of vertical compression, the critical buckling load is (Spagnoli, 2003),

$$L_c = \frac{2\pi Eh^2}{\sqrt{3(1-\nu^2)}}\cos^2\alpha, \tag{15}$$

from which the critical bucking stress along s direction σ_{sc} can be deduced as $\frac{Eh\cot\alpha}{s\sqrt{3(1-\nu^2)}}$. For a hydrostatically compressed cone, the critical pressure for causing radial buckling is estimated as (Liu et al., 1987),

$$-P_c = 3.15E\left(\frac{h}{s_b}\right)^{2.5}\cot^{1.5}\alpha\sqrt{\frac{1}{(1-\nu)^{3/2}}}. \tag{16}$$

2.5. MD simulations

Finally, MD simulations are used to verify results obtained by these continuum theories. Details of the computations and methods are provided in the section II of SI. For ease of comparison later, we use MD-compatible parameters in all the continuum theories, i.e. $Eh = 243$ N/m, $\nu = 0.397$, $D = Eh^3/12(1\text{-}\upsilon^2) = 1.41$ eV (Brenner et al., 2002), and extract E and h from Eh and D. Notice the slight anisotropy induced by curvature (Chang, 2010) is ignored here. DFT-compatible parameters (Kudin et al., 2001) are also tested, yielding similar results, as shown in Fig. S7b and S7c in SI.

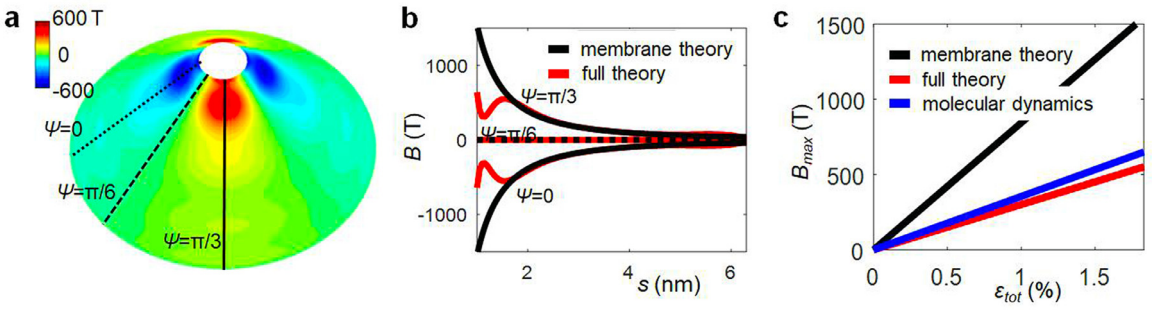

Fig. 2. *P*-mag field B in compressed cones. (a) Map of B calculated by full shell theory in the cone at $\varepsilon_{\text{tot}} = 1.8\%$. (b) Distribution of B along three meridians, $\psi = 0$, $\psi = \pi/6$ and $\psi = \pi/3$. (c) Maximum B achieved in the cone as a function of ε_{tot}. The results from membrane theory, full shell theory and molecular dynamics simulations are shown.

3. Results for vertical loads

We first take the CNC with disclination angle $\Delta = 2\pi/3$ Fig. 1a) as a model system to discuss our results. The corresponding tapering angle is $\alpha = 41.8°$, and s is set to vary from 1 to 6.3 nm. As mentioned, the cone is subject to structural instability when the vertical load is over a critical value, leading to a nonlinear mechanical response beyond the scope of this paper. MD simulation estimates a critical ε_s of ~4% at the cone's top and ~0.7% at its bottom (Fig. 1c), far below the breaking strain of graphene. Converting these local strains into a vertical total strain yields $\varepsilon_{\text{tot}} = 1.83\%$ from MD simulation and 2% from Eqs. (5) and (15). This critical strain increases with decreasing the Δ and s_b, according to the shell theory (Fig. 1d). We ensure that the studied strains are no larger than the critical value.

For a cone with $\Delta = 2\pi/3$, the distribution of B at $\varepsilon_{\text{tot}} = 1.8\%$ is presented in Fig. 2a and b, where the intensity of $|B|$ is maximized near the top end of the cone, reaching 550 T by the full shell theory and 650 T by MD simulation at $s = 1.5$ nm. Away from the cone's top, the intensity of $|B|$ decays by s^{-2} along the meridian but still reaches 175 T at $s = 3$ nm and 63 T at $s = 6$ nm. In other words, a large portion of the cone's surface exhibits distinctly stronger *p*-mag fields than those in other strained carbon nanostructures (Guinea et al., 2010a; Low and Guinea, 2010; Zhang et al., 2014a). Of more significance is that the maximum local strain required for these fields is merely 4.1%, much smaller than 15–20% for attaining similar strength of B in deformed graphene ribbons (Zhang et al., 2014a; Zhu et al., 2015). This strong coupling between strain and charge carriers results from the unique topology of CNC, which elicits a divergence of strains near the CNC top.

Another characteristic of B is a periodic distribution in the θ direction, originated from the sinusoidal term $\cos 3\psi$ in Eq. (3). When $\Delta = 2\pi/3$, ψ ranges from 0 to $4\pi/3$, which results in two periods of B pattern in the θ direction. The pattern is quantitatively supported by showing B along three principal meridians, i.e. $\psi = 0$, $\pi/6$ and $\pi/3$ in Fig. 2b. B in the $\psi = 0$ and $\pi/3$ directions have the same magnitude but opposite signs; whereas B simply disappears in the $\psi = \pi/6$ direction. The results suggest that B disappears along all the meridians with $\psi = \pi/6 + n\pi/3$ ($n = 0 \sim 3$). These characters of B are reproduced at smaller ε_{tot}, except that $B_{\max}$ decreases linearly with ε_{tot} (Fig. 2c).

Such a periodic distribution of B along the θ direction is unique to the conic geometry due to its circular character. Our analysis reveals that the distribution of B should exhibit $3(1 - \Delta/2\pi)$ periods. A cone with $\Delta = 4\pi/3$ has only one period for B, while graphene, an extreme case with $\Delta = 0$, has three periods, in line with previous results in graphene with designed strain along three main crystallographic directions (Guinea et al., 2010b). In contrast, when n in $\Delta = n\pi/3$ is odd (i.e. $n = 1$, 3, 5), the cone will have fractional number of periods, with an abrupt switch of B from positive to negative along a certain meridian (see an example in Fig. S7d). Thus, straining these cones can induce an infinitely large gradient of B, which then causes a flip of direction of electronic procession therein. The abrupt switch of B can occur in any CNCs without mirror symmetry and may be utilized for novel devices based on a large gradient of magnetic fields.

In experiments, it is also feasible to stretch a cone vertically by, for example, adhering the cone on a substrate and then lifting the cone's apex by a pin going through an aperture in the substrate underneath the cone (Fig. S8). Since the *p*-mag fields linearly depend on all the strain components, the patterns of strain components (i.e. ε_s and ε_θ) and *p*-mag field B will be identical to that in the compressed cone except that their signs become opposite (see results in Fig. S9). Notably, the stretch avoids the buckling issue of CNCs, so that the cone can withstand a larger $|\varepsilon_{\text{tot}}|$ to achieve a higher $B_{\max}$ than that under the compression. For example, stretching the same cone shown in Fig. 2a (now the cone's apex is not truncated but fixed to the pin) by 5.4% ends up a $B_{\max}$ of up to 1650 T near to the apex, where the maximal ε_s increases to ~12%.

We notice that B is highly concentrated around the cone's top end and fluctuates in the θ direction. Such a non-uniform B distribution limits potential application. This issue can be circumvented by increasing the truncated depth s_a. We thus turn to examine the dependence of B on s_a. For a cone with $\Delta = 2\pi/3$, $s_b = 6.3$ nm and $\varepsilon_{\text{tot}} = 1\%$, the distribution of B with $s_a = 3$ nm is shown in Fig. 3a, where B is indeed much more dispersive than that shown in Fig. 2a with $s_a = 1$ nm. In this case, $|B|$ decreases from the maximum of 72 T along the circle at $s = 4.2$ nm to 54 T along that at $s = 6$ nm. To capture a broader picture, we map in Fig. 3b the variation of B against change in s_a and s, all recorded along $\psi = \pi/3$ that gives

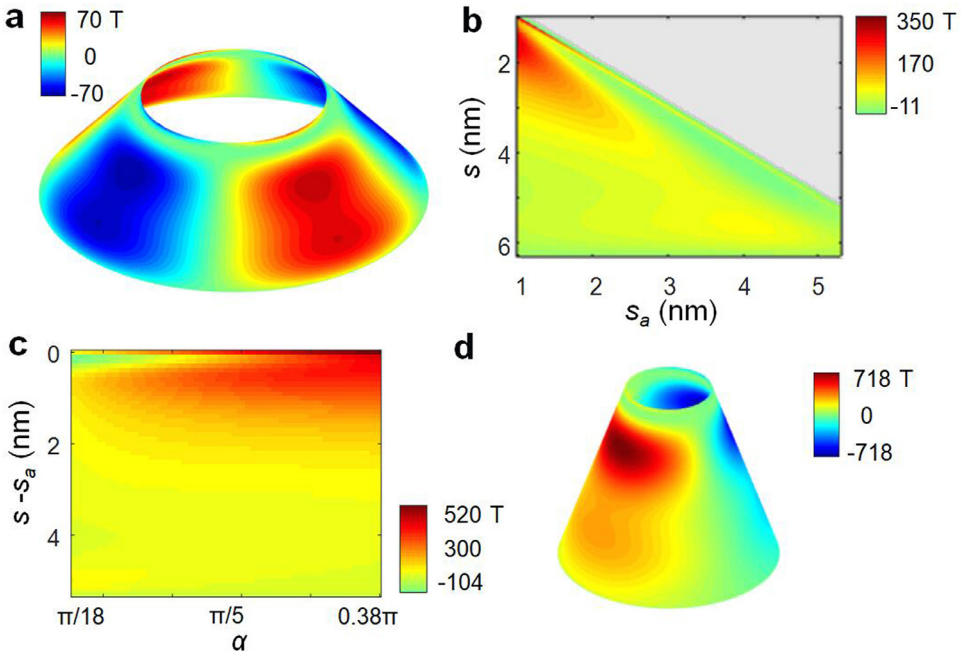

Fig. 3. Dependence of *p*-mag fields on the cone geometry. (a) Map of field in a truncated cone with $\Delta = 2\pi/3$, $s_a = 3$ nm, $s_b = 6.3$ nm and $\varepsilon_{tot} = 1\%$. (b) Effect of s_a on the field in the $\psi = \pi/3$ direction. Parameters other than s_a are the same to (a). (c) Effect of the apex angle α on the field with $r_a = 0.67$ nm $s_b - s_a = 5.3$ nm and $\varepsilon_{tot} = 1\%$. (d) Map of the field in a cone with $\Delta = 4\pi/3$ and $\varepsilon_{tot} = 4.2\%$. Other parameters are the same to (c). All strains in (a–d) are below the critical value for buckling of cones.

maximal *B*. Indeed, *B* exhibits a smoother decay with *s* in more truncated cone. B_{max} decreases from 303 T in the cone with $s_a = 1.0$ nm to 43 T in the one with $s_a = 5.3$ nm. While B_{max} decreases markedly with increasing s_a, the change of *B* at the cone's bottom is limited. The dependence of B_{max} on s_a and s_b can be deduced as proportional to $s_a^{-2}/\ln(s_b/s_a)$ according to Eqs. (5) and (6), consistent with the trend in Fig. 3b.

We further study the dependence of *B* distribution on α. Here, α is continuously variable since a CNC can form at an arbitrary tapering angle α if aided by a grain boundary. We note that electronic property near the grain boundary is modified (Yazyev and Louie, 2010; Zhang et al., 2014c), but the Dirac electronic state in perfect lattice regions of the cone remains effective for the strain-induced *B*. For this purpose, we keep s_b-$s_a = 5.3$ nm and $r_a = 0.67$ nm (the radius of the cone's top cross-section) while varying α from $\pi/18$ to $\sim 2\pi/5$, uniformly compressed by $\varepsilon_{tot} = 1\%$. The CNCs with $\alpha > 0.38\pi$ are not considered since they will be buckled even at $\varepsilon_{tot} = 1\%$. *B* recorded along $\psi = \pi/3$ as a function of α is depicted in Fig. 3c, where two trends are clear. First, B_{max} near the apex increases with α, from 92 T at $\alpha = \pi/18$ to 522 T when α approaches $2\pi/5$. Second, the decay of *B* is smoother (except for areas near cone's ends) as the cone is more like a carbon nanotube. For example, along $\psi = \pi/3$, *B* decays from 522 T to 11 T when $\alpha = 0.38\pi$, but from 92 T to 26 T when $\alpha = \pi/18$. Apparently, a high intensity of *B* corresponds to a poor homogeneity in its distribution. Is there a cone geometry that enables a good tradeoff between the intensity and homogeneity of *B*? The cone with $\alpha = 19.5°$ (i.e. $\Delta = 4\pi/3$) and $r_a = 0.67$ nm is shown to meet this condition. If other parameters of this cone are the same as that in Fig. 3c, *B* decays from 171 T near the top to 33 T near the bottom at $\varepsilon_{tot} = 1\%$ (Fig. 3d).

The dependence of *B* on s_b is also studied. For the model, we keep $s_a = 1$ nm, $\Delta = 2\pi/3$ and $\varepsilon_{tot} = 1\%$. *B* recorded along $\psi = \pi/3$ as a function of s_b reveals that *B* always decays with *s* but B_{max} increases with increasing s_b (see Fig. S7e). For example, B_{max} increases from 350 T in the cone with $s_b = 3.3$ nm to 680 T in the cone with $s_b = 9.3$ nm. This is similar to the trend in Fig. 3b, where the longer cone is shown to exhibit a higher B_{max}.

4. Results for hydrostatic loads

The inhomogeneity of *B* distribution always exists in the compressed CNCs, determined by the cone's topology. This fact motivates us to explore a new way to generate uniform *B* on the cones. We resort to a hydrostatic pressure that can evenly exert force onto a whole structure and has been applied to carbon nanostructures for studying novel mechanics at nanoscale (Alencar et al., 2017; Guo and Guo, 2007; Xu et al., 2008). A CNC can withstand hydrostatic inflation and compression when its apex is not truncated. For capturing the basic physics, we focus on the hydrostatic inflation, which can be realized by mounting the cone on a sticky substrate and inflating from an aperture underneath, as illustrated in Fig. 4a. Such technology has been successfully applied to create nanobubbles in graphene on substrates (Boddeti et al., 2013). In MD simulations, the hydrostatic pressure is implemented by applying a uniform force on each atom, which is perpendicular to the cone surface

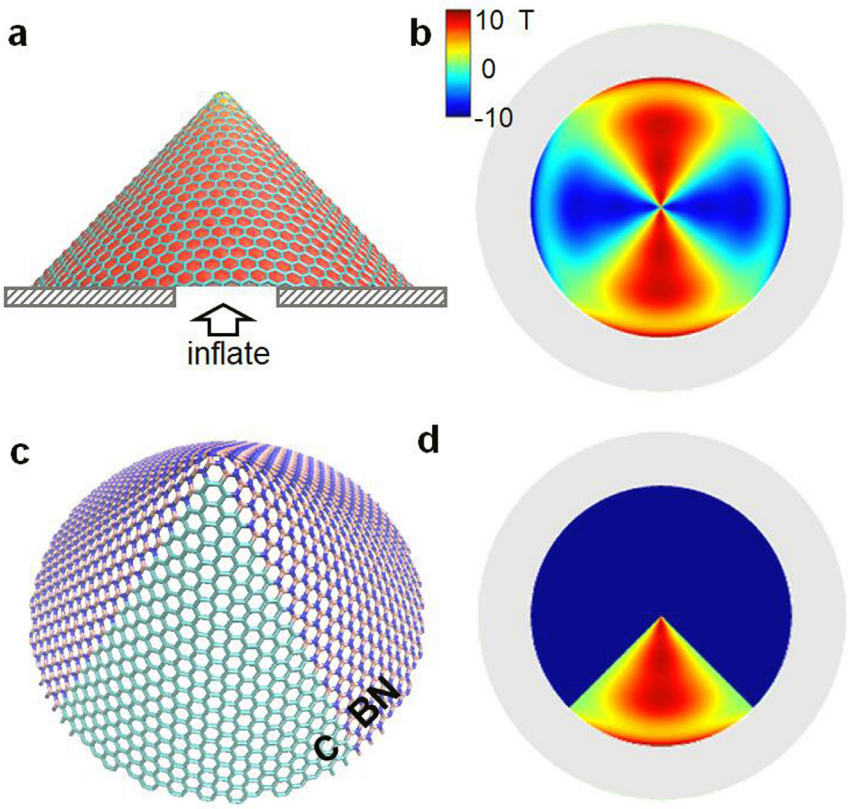

Fig. 4. *P*-mag fields in inflated CNCs. (a) Schematic illustration of inflating a nanocone with pressure *P*. (b) Top view of the field distribution at $P=1$ GPa. The fields in the region near the bottom edge are removed. (c) A schematic model of a hybrid cone comprised of carbon and h-BN sectors. (d) Top view of the field distribution in an inflated hybrid cone ($P=1$ GPa).

while pointing outward. Based on the membrane theory, B is obtained by Eq. (10). It shows that B is a constant along the direction of a given ψ. This analytical solution verified our idea but failed to describe B near the cone ends. More accurate numerical results are obtained using the full shell theory and discussed as below.

For demonstration, we set $\Delta=2\pi/3$, $s\in$ [0, 6.3] nm and $P=1$ GPa that is feasible to realize in experiments (Boddeti et al., 2013). Unlike the vertical compression, the hydrostatic pressure makes the strain maximized at the cone's bottom, where ε_θ and ε_s are 1.5% and 0.8%, respectively (Fig. S12). Such a strain pattern results in a distinct distribution of B along the meridian (Fig. 4b and Fig. S11). The remarkable feature is the appearance of nearly constant B in the region of $s\leq 3.1$ nm, where B ranges from 16.9 to 18.6 T (B near the cone's bottom is shaded due to the edge effect). This distribution of B is more uniform than that induced by vertical compression, even if fluctuation remains along the θ direction. Eq. (10) also shows that increasing α can further enhance the intensity of B. The numerical results are verified by MD simulation (Figs. S12 and S13). Increasing the pressure P further enhances the intensity of B, but the effect of cone's ends is more significant. The cone will adopt a shape with cambered meridians once P exceeds 1 GPa (Fig. S14), resulting in a large discrepancy between the results from the full shell theory and MD simulation (Figs. S12 and S13).

Having realized a constant B along the meridian, we proceed by suggesting two ways to restrict its fluctuation in the θ direction. One way is to use a cone with $\alpha<9.5°$ (i.e. $\Delta>5\pi/3$), which narrows the B distribution along the θ direction to be less than half a period, ending up the same sign of B across the whole cone. The other way is to make a hybrid cone comprised of graphene and h-BN sectors as shown in Fig. 4c, which should be feasible to synthesize by current experimental techniques, notably by employing methods of growing graphene–BN heterostructures (Gao et al., 2013; Han et al., 2013; Kim et al., 2015; Liu et al., 2014) yet using a conic substrate (Yu et al., 2017). Under inflation, such a hybrid cone is benefited by the similar mechanical properties between graphene and h-BN (Nag et al., 2010; Wu et al., 2013). Since the h-BN sector is insulating, B is confined in the graphene sector, with a distribution controlled by varying the sector angle $\psi_{\rm gr}$. According to Eq. (3), B can have the same sign in the graphene sector as long as $\psi_{\rm gr}\leq\pi/3$. This result is conceptually demonstrated in a compressed truncated hybrid cone (Fig. S15) and an inflated hybrid cone without truncation (Fig. 4d), both with $\psi_{\rm gr}=\pi/3$. The inflated hybrid cone shows a uniform distribution of B all the way up to the apex. Yet, owing to the imposed clamped condition by substrate, B undergoes a sharp increase near the cone's bottom (Fig. S10), which is shaded in grey as well.

We also check the case of hydrostatic compression for a pristine CNC and obtain similar distributions of ε_s, ε_θ and B except that their signs turn opposite (Fig. S16). Nevertheless, the hydrostatic compression readily causes a structural buckling in the CNCs, with a critical pressure of only ∼0.4 GPa by Eq. (16) for the cone shown in Fig. 4a. As such, the intensity of induced *p*-mag fields is limited to several Tesla.

Unlike simulations, realizing an inflated CNC requires to fill the cone with gas molecules (e.g. N_2 or Ar) in experiments. To examine possible effect of molecules, we perform density functional theory (DFT) calculations (Kresse and Furthmüller, 1996; Perdew et al., 1996) and find that the band structures of graphene are little affected by adsorbed N_2 or Ar (Fig. S19). Moreover, the strain gradient can be persisted in the cone by the pressure of molecules. The coexistence of strain gradient and Dirac fermion will ensure the appearance of *p*-mag fields in the cone inflated with chemically inert gas molecules.

5. Conclusions

In summary, our extensive continuum analyses and atomistic simulations have shown that CNCs exhibit peculiar coupling between mechanical strain and charge carriers, resulting in extreme *p*-mag fields. The fields reach hundreds of Tesla under a vertical strain of merely ∼2%, in contrast to other carbon nanostructures that require tensile strains up to ∼15% to achieve the same order of field strength. The field decays along the meridians while fluctuates periodically along the circumference. The distribution and intensity of the fields can be tailored by varying the cone's geometry. Alternatively, the decay of *p*-mag fields in the meridian can be suppressed by applying a hydrostatic pressure, while the field fluctuation along the circumference can be engineered using a hybrid cone comprised of graphene and h-BN sectors. As an easy-to-obtain material, the CNCs hold great promise for generating *p*-mag fields in a cost-effective way and provide a new platform for exploring carrier dynamics in extremely strong magnetic fields.

Acknowledgments

This work was supported by National Natural Science Foundation of China (11772153, 51535005, 51472117, 11802121), the Research Fund of State Key Laboratory of Mechanics and Control of Mechanical Structures (MCMS-0416G0, MCMS-0417G01, MCMS-0417G02, MCMS-0417G03), Natural Science Foundation of Jiangsu Province (BK20180416), the Fundamental Research Funds for Central Universities (NP2017101, NC2018001, NE2018002, NS2018004), and the support of Youth Thousand Talents Program.

Supplementary materials

Supplementary material associated with this article can be found, in the online version, at doi:10.1016/j.jmps.2018.09.037.

References

Abedpour, N., Asgari, R., Guinea, F., 2011. Strains and pseudomagnetic fields in circular graphene rings. Phys. Rev. B 84, 115437.
Alencar, R.S., Cui, W.W., Torres-Dias, A.C., Cerqueira, T.F.T., Botti, S., Marques, M.A.L., Ferreira, O.P., Laurent, C., Weibel, A., Machon, D., Dunstan, D.J., Souza, A.G., San-Miguel, A., 2017. Pressure-induced radial collapse in few-wall carbon nanotubes: a combined theoretical and experimental study. Carbon 125, 429–436.
Boddeti, N.G., Liu, X.H., Long, R., Xiao, J.L., Bunch, J.S., Dunn, M.L., 2013. Graphene blisters with switchable shapes controlled by pressure and adhesion. Nano Lett. 13, 6216–6221.
Brenner, D.W., Shenderova, O.A., Harrison, J.A., Stuart, S.J., Ni, B., Sinnott, S.B., 2002. A second-generation reactive empirical bond order (REBO) potential energy expression for hydrocarbons. J. Phys.: Condens. Matter 14, 783–802.
Cano-Marquez, A.G., Schmidt, W.G., Ribeiro-Soares, J., Cancado, L.G., Rodrigues, W.N., Santos, A.P., Furtado, C.A., Autreto, P.A.S., Paupitz, R., Galvao, D.S., Jorio, A., 2015. Enhanced mechanical stability of gold nanotips through carbon nanocone encapsulation. Sci. Rep (UK) 5, 10408.
Castro-Villarreal, P., Ruiz-Sánchez, R., 2017. Pseudomagnetic field in curved graphene. Phys. Rev. B 95, 125432.
Chang, T., 2010. A molecular based anisotropic shell model for single-walled carbon nanotubes. J. Mech. Phys. Solids 58, 1422–1433.
Cui, W.C., Pei, J.H., Zhang, W., 2001. A simple and accurate solution for calculating stresses in conical shells. Comput. Struct. 79, 265–279.
Dumitrica, T., Hua, M., Yakobson, B.I., 2006. Symmetry-, time-, and temperature-dependent strength of carbon nanotubes. Proc. Natl. Acad. Sci. USA 103, 6105–6109.
Gao, Y.B., Zhang, Y.F., Chen, P.C., Li, Y.C., Liu, M.X., Gao, T., Ma, D.L., Chen, Y.B., Cheng, Z.H., Qju, X.H., Duan, W.H., Liu, Z.F., 2013. Toward single-layer uniform hexagonal boron nitride-graphene patchworks with zigzag linking edges. Nano Lett. 13, 3439–3443.
Ghosh, P., Yusop, M.Z., Satoh, S., Subramanian, M., Hayashi, A., Hayashi, Y., Tanemura, M., 2010. Transparent and flexible field electron emitters based on the conical nanocarbon structures. J. Am. Chem. Soc 132, 4034.
Guinea, F., Geim, A.K., Katsnelson, M.I., Novoselov, K.S., 2010a. Generating quantizing pseudomagnetic fields by bending graphene ribbons. Phys. Rev. B 81, 035408.
Guinea, F., Katsnelson, M.I., Geim, A.K., 2010b. Energy gaps and a zero-field quantum Hall effect in graphene by strain engineering. Nat. Phys. 6, 30–33.
Guo, Y.F., Guo, W.L., 2007. Reassembly of single-walled carbon nanotubes into hybrid multilayered nanostructures inside nanotube extruders. Phys. Rev. B 76, 045404.
Han, G.H., Rodriguez-Manzo, J.A., Lee, C.W., Kybert, N.J., Lerner, M.B., Qi, Z.J., Dattoli, E.N., Rappe, A.M., Drndic, M., Johnson, A.T.C., 2013. Continuous growth of hexagonal graphene and boron nitride in-plane heterostructures by atmospheric pressure chemical vapor deposition. ACS Nano 7, 10129–10138.
Hashimoto, A., Yorimitsu, H., Ajima, K., Suenaga, K., Isobe, H., Miyawaki, A., Yudasaka, M., Iijima, S., Nakamura, E., 2004. Selective deposition of a gadolinium(III) cluster in a hole opening of single-wall carbon nanohorn. Proc. Natl. Acad. Sci. USA 101, 8527–8530.
Jaszczak, J.A., Robinson, G.W., Dimovski, S., Gogotsi, Y., 2003. Naturally occurring graphite cones. Carbon 41, 2085–2092.
Kim, G., Lim, H., Ma, K.Y., Jang, A.R., Ryu, G.H., Jung, M., Shin, H.J., Lee, Z., Shin, H.S., 2015. Catalytic conversion of hexagonal boron nitride to graphene for in-plane heterostructures. Nano Lett. 15, 4769–4775.
Kim, K.J., Blanter, Y.M., Ahn, K.H., 2011. Interplay between real and pseudomagnetic field in graphene with strain. Phys. Rev. B 84, 081401.

Kim, K.S., Zhao, Y., Jang, H., Lee, S.Y., Kim, J.M., Kim, K.S., Ahn, J.H., Kim, P., Choi, J.Y., Hong, B.H., 2009. Large-scale pattern growth of graphene films for stretchable transparent electrodes. Nature 457, 706–710.
Kim, Y.A., Hayashi, T., Osawa, K., Endo, M., Dresselhaus, M.S., 2003. Cone-type multi-shell in the hollow core of multi-wall carbon nanotube. Chem. Phys. Lett. 367, 537–540.
Kresse, G., Furthmüller, J., 1996. Efficiency of *ab-initio* total energy calculations for metals and semiconductors using a plane-wave basis set. Comput. Mater. Sci. 6, 15–50.
Kudin, K.N., Scuseria, G.E., Yakobson, B.I., 2001. C2F, BN, and C nanoshell elasticity from *ab initio* computations. Phys. Rev. B 64, 235406.
Lavin, J.G., Subramoney, S., Ruoff, R.S., Berber, S., Tomanek, D., 2002. Scrolls and nested tubes in multiwall carbon nanotubes. Carbon 40, 1123–1130.
Levy, N., Burke, S.A., Meaker, K.L., Panlasigui, M., Zettl, A., Guinea, F., Neto, A.H.C., Crommie, M.F., 2010. Strain-induced pseudo-magnetic fields greater than 300 tesla in graphene nanobubbles. Science 329, 544–547.
Liew, K.M., Wei, J.X., He, X.Q., 2007. Carbon nanocones under compression: buckling and post-buckling behaviors. Phys. Rev. B 75, 195435.
Liu, B., Jiang, H., Johnson, H.T., Huang, Y., 2004. The influence of mechanical deformation on the electrical properties of single wall carbon nanotubes. J. Mech. Phys. Solids 52, 1–26.
Liu, F., Ming, P., Li, J., 2007. *Ab initio* calculation of ideal strength and phonon instability of graphene under tension. Phys. Rev. B 76, 064120.
Liu, H.W., Lin, J.X., Cao, M.L., 1987. Theory of Plates and Shells. Zhejiang University, Hangzhou [in Chinese].
Liu, L., Park, J., Siegel, D.A., McCarty, K.F., Clark, K.W., Deng, W., Basile, L., Idrobo, J.C., Li, A.P., Gu, G., 2014. Heteroepitaxial growth of two-dimensional hexagonal boron nitride templated by graphene edges. Science 343, 163–167.
Liu, L.C., 2018. Pseudo-magnetic fields of strongly-curved graphene nanobubbles. Int. J. Mod. Phys. B 32, 1850137.
Low, T., Guinea, F., 2010. Strain-induced pseudomagnetic field for novel graphene electronics. Nano Lett. 10, 3551–3554.
Lu, X., Yang, Q., Xiao, C., Hirose, A., 2006. Field electron emission of carbon-based nanocone films. Appl. Phys. A: Mater. 82, 293–296.
Merkulov, V.I., Melechko, A.V., Guillorn, M.A., Lowndes, D.H., Simpson, M.L., 2001. Sharpening of carbon nanocone tips during plasma-enhanced chemical vapor growth. Chem. Phys. Lett. 350, 381–385.
Naess, S.N., Elgsaeter, A., Helgesen, G., Knudsen, K.D., 2009. Carbon nanocones: wall structure and morphology. Sci. Technol. Adv. Mater. 10, 065002.
Nag, A., Raidongia, K., Hembram, K.P.S.S., Datta, R., Waghmare, U.V., Rao, C.N.R., 2010. Graphene analogues of BN: novel synthesis and properties. ACS Nano 4, 1539–1544.
Perdew, J.P., Burke, K., Ernzerhof, M., 1996. Generalized gradient approximation made simple. Phys. Rev. Lett. 77, 3865–3868.
Ramezani Masir, M., Moldovan, D., Peeters, F.M., 2013. Pseudo magnetic field in strained graphene: revisited. Solid State Commun. 175-176, 76–82.
Spagnoli, A., 2003. Koiter circles in the buckling of axially compressed conical shells. Sci. Technol. Adv. Mater. 40, 6095–6109.
Wei, C.Y., Srivastava, D., 2004. Nanomechanics of carbon nanofibers: structural and elastic properties. Appl. Phys. Lett. 85, 2208–2210.
Wu, J., Wang, B., Wei, Y., Yang, R., Dresselhaus, M., 2013. Mechanics and mechanically tunable band gap in single-layer hexagonal boron-nitride. Mater. Res. Lett. 1, 200–206.
Wu, J., Wei, Y., 2013. Grain misorientation and grain-boundary rotation dependent mechanical properties in polycrystalline graphene. J. Mech. Phys. Solids 61, 1421–1432.
Xu, Z., Zheng, Q., 2018. Micro- and nano-mechanics in China: a brief review of recent progress and perspectives. Sci. China Phys. Mech. Astron. 61, 074601.
Xu, Z.P., Wang, L.F., Zheng, Q.S., 2008. Enhanced mechanical properties of prestressed multi-walled carbon nanotubes. Small 4, 733–737.
Yakobson, B.I., 1998. Mechanical relaxation and "intramolecular plasticity" in carbon nanotubes. Appl. Phys. Lett. 72, 918–920.
Yang, Q., Chen, W., Xiao, C., Hirose, A., Sammynaiken, R., 2005. Simultaneous growth of well-aligned diamond and graphitic carbon nanostructures through graphite etching. Diam. Relat. Mater. 14, 1683–1687.
Yazyev, O.V., Louie, S.G., 2010. Topological defects in graphene: dislocations and grain boundaries. Phys. Rev. B 81, 195420.
Yeh, N.C., Teague, M.L., Yeom, S., Standley, B.L., Wu, R.T.P., Boyd, D.A., Bockrath, M.W., 2011. Strain-induced pseudo-magnetic fields and charging effects on CVD-grown graphene. Surf. Sci. 605, 1649–1656.
Yu, H., Gupta, N., Hu, Z.L., Wang, K., Srijanto, B.R., Xiao, K., Geohegan, D.B., Yakobson, B.I., 2017. Tilt grain boundary topology induced by substrate topography. ACS Nano 11, 8612–8618.
Yudasaka, M., Iijima, S., Crespi, V.H., 2008. Single-wall carbon nanohorns and nanocones. Top. Appl. Phys. 111, 605–629.
Zhang, D.B., Seifert, G., Chang, K., 2014a. Strain-induced pseudomagnetic fields in twisted graphene nanoribbons. Phys. Rev. Lett. 112, 096805.
Zhang, G., Jiang, X., Wang, E., 2003. Tubular graphite cones. Science 300, 472–474.
Zhang, T., Li, X., Gao, H., 2014b. Defects controlled wrinkling and topological design in graphene. J. Mech. Phys. Solids 67, 2–13.
Zhang, Z., Yang, Y., Xu, F., Wang, L., Yakobson Boris, I., 2014c. Unraveling the sinuous grain boundaries in graphene. Adv. Funct. Mater. 25, 367–373.
Zhu, S.Z., Stroscio, J.A., Li, T., 2015. Programmable extreme pseudomagnetic fields in graphene by a uniaxial stretch. Phys. Rev. Lett. 115, 245501.